Journal of
Marine Science and Engineering

MDPI

Article

Behavior of PIP Slip Joint in the Offshore Wind Monopile under Combined Load Considering Local Buckling

Md Ariful Islam [1], Sajid Ali [1], Hongbae Park [2] and Daeyong Lee [2,*]

[1] Energy Innovation Research Center for Wind Turbine Support Structures, Kunsan National University, 558 Daehak-ro, Gunsan-si 54150, Jeollabuk-do, Republic of Korea; arifriyad@kunsan.ac.kr (M.A.I.); sajid_ali@kunsa.ac.kr (S.A.)
[2] Department of Wind Energy, The Graduate School of Kunsan National University, 558 Daehak-ro, Gunsan-si 54150, Jeollabuk-do, Republic of Korea; dcv003@naver.com
* Correspondence: daeyong.lee@kunsan.ac.kr; Tel.: +82-10-4490-0980

Abstract: Considering the practical conditions, it has been observed that the support structures of wind turbines inevitably experience bending and axial compression, both during the installation phase and throughout their operational lifespan. The monopile is the most commonly utilized support structure for offshore applications and a reliable method for creating a detachable section within these structures is using a Pile-in-Pile (PIP) slip joint. Consequently, the behavior of PIP slip joints, under combined axial compression and bending, has been meticulously investigated. To facilitate a thorough analysis, overlapping lengths proportional to the pile diameters have been used, encompassing three distinct variations. This approach allows for a comprehensive understanding of structural integrity and performance under varying stress conditions, which are comprehensively understood and accounted for in design considerations. The current study builds upon assessing the pure bending characteristics of slip joints in cylindrical hollow section (CHS) structures. Additionally, two ring stoppers have been strategically employed inside the piles to withstand the axial load. Furthermore, the complexity of the pressure acting in the overlapping length, attributed to the frictional coefficient in that region, has been carefully addressed. The current research also encompasses a comprehensive overview of the P-M envelopes for the existing arrangements, with a particular focus on non-linear buckling, which is known to significantly influence the performance of tubular structures. Finally, a design equation was introduced to concisely describe the behavior of the components and compare it with other design equations provided by an established code.

Keywords: PIP slip joint; circular hollow section; overlapping length; ring stopper; combined load; monopile

Citation: Islam, M.A.; Ali, S.; Park, H.; Lee, D. Behavior of PIP Slip Joint in the Offshore Wind Monopile under Combined Load Considering Local Buckling. *J. Mar. Sci. Eng.* **2024**, *12*, 1423. https://doi.org/10.3390/jmse12081423

Academic Editors: José António Correia and Rodolfo T. Gonçalves

Received: 20 June 2024
Revised: 6 August 2024
Accepted: 15 August 2024
Published: 17 August 2024

1. Introduction

The design of the monopile is a pivotal factor in determining the maximum height of an offshore wind turbine. This design is critical for ensuring the safe, efficient, and economical operation of offshore wind turbines, significantly as they increase in height and are subjected to more demanding environmental conditions. It requires a balance of engineering, environmental science, and economics to achieve the best outcome for sustainable energy production [1]. In the monopile design, tubular steel structures are essential due to their robustness and ability to withstand dynamic loads and vibrations. They offer advantages such as prefabrication off-site, requiring less on-site labor, and easier mounting of turbine components. Additionally, these structures allow wind turbines to be positioned at optimal heights, maximizing energy production from faster winds at higher altitudes [2]. Overall, tubular structures play a crucial role in ensuring wind turbines' safety, longevity, and energy efficiency for sustainable energy production. Innovation in tubular sections analysis is not only vital in the tower in the tower structure, but also in the support structure system like the monopiles (as shown in Figure 1), jacket structures, or in the legs

of jack-up barge arrangements. Hence, an optimum and simplified installation process of these support systems can also reduce the construction hassles and costs, ensure structural integrity, and enable innovation in wind energy projects [3]. Because of its significance, "DNV-ST-0126 Support structures for wind turbines" provides general principles and guidelines for the structural design, installation, and in-service inspection of wind turbine support structure systems [4].

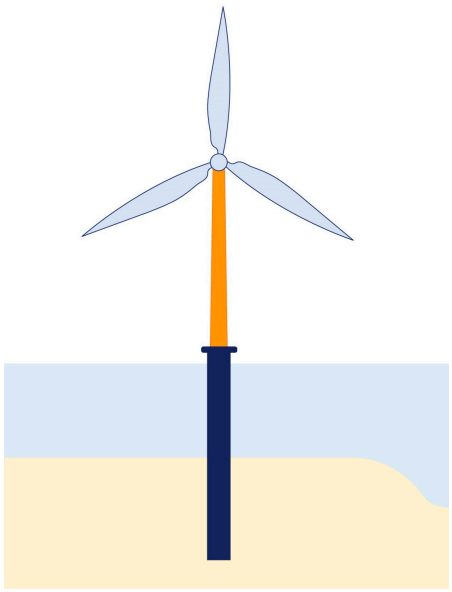

Figure 1. Circular hollow sections (CHS) consisting of a wind tower and monopile substructure.

When making decisions about energy system investments, it is essential to consider all aspects of planning, development, and construction. In general, it was found that the initial cost of a wind turbine system covered one-fourth of the total cost. Therefore, designers should prioritize building a robust and cost-effective structure in the planning phase [5,6]. A detachable tubular structure for a wind turbine tower offers several advantages in a support structure system. These benefits include faster and easier installation, reduced construction costs, and minimized environmental impact. Additionally, it enables improved transportation and assembly, increased robustness, better interaction with the wind, and cost savings that align with environmental considerations by reducing energy consumption and promoting sustainable practices. Furthermore, in times of emergency, the mobility of the structure gives engineers an advantage in preventing potential damage during natural calamities. However, due to limited studies, the potential of detachable joints in circular hollow section (CHS) structures still needs to be explored. Connections for hollow sections in steel construction are achieved mainly through welding or bolting. Welded circular hollow section joints are used for longitudinal joints and connecting braces to continuous chords, as Ummenhofer et al. (2002) [7] used in their study.

On detachable tubular structures the most commonly used method is to use pre-stressed bolt in the flange of the CHS structure. The creation of L-type flanges is believed to be connected to the standardization initiatives for pressure vessels and piping systems during the Industrial Revolution. In the early 20th century, the American Society of Mechanical Engineers (ASME) [8] spearheaded establishing and documenting flange standards, including L-type flanges, laying the groundwork for safety and quality in engineering practices. In a recent study, Tran et al. (2023) [9] also developed a finite element model of a 5 MW L-type flange joint and verified its accuracy through experimental test results. They investigated the influences of geometrical imperfections (such as flange and tower-sided gaps) on the structural response using the same loading conditions and material properties. Another significant probabilistic study was conducted on the two-planar local joint flexibility by Ahmadi and Mayeli in 2018 [10]. In their study, nine theoretical probability

density function curves (PDFs) were prepared and fitted to the developed histograms. The maximum likelihood (ML) method was then applied to evaluate the parameters of the fitted PDFs. However, these connections are not easily detachable, so it is imperative to discover new hybrid connections that offer easier installation and mobility when needed. As a result, in a previous study, Islam et al. (2023) [11] tried to develop a detachable joint named Pile-in-Pile (PIP) slip joint and explored the structural behavior under pure bending. For further development in this research, the response of a PIP slip joint subjected to bending and axial compression, considering perturbation, has been analyzed.

PIP slip joints are a one-of-a-kind new structural innovation that allows the contact surfaces of the CHSs to slide apart from each other, as demonstrated in Figure 2. Some prior studies found that moment capacity, self-centering ability, and rotational stiffness are fundamental for analyzing the support structure system [11]. Therefore, in the first step, the behavior of the PIP slip joint was investigated for a pure bending case to determine the optimum overlapping length for this CHS structure arrangement. For the next step, the combined loading of axial force and bending in wind turbine structures is crucial for several reasons. The combined loading of axial force (due to gravity and wind loads) and bending (due to wind-induced moments) affects the overall efficiency of the tubular structures. According to NORSOK N-004, tubular members subjected solely to axial tension, axial compression, bending, shear, or hydrostatic pressure should be designed to meet the strength and stability requirements. Tubular members subjected to combined loads without hydrostatic pressure should also be designed to meet the strength and stability requirements [12]. By considering both axial and bending loads, engineers can also optimize the design to minimize material usage while ensuring structural integrity. Likewise, buckling is another critical failure mode for slender structures especially for CHS arrangements. Combined axial and bending loads influence buckling behavior and hence proper design accounts for buckling resistance need to be considered to prevent the possibility of failure. Wind-induced bending moments can also cause sliding between tower segments (e.g., flanges or slip joints), which can impact the overall tower stability. Analyzing these sliding distances ensures a safe operation and prevents excessive wear. Ideally, in the current study, the overlap will resist external bending, and two ring stoppers will be used inside the joint area to resist axial compression. Three different overlapping arrangements have been assessed thoroughly, while the dimensions of the ring stoppers remain unchanged. Local buckling near the overlapping area was also extensively studied as that part was found to be most interesting. After conducting a thorough analysis, we developed design equations for the entire system and its components. These will be compared with the well-established existing code.

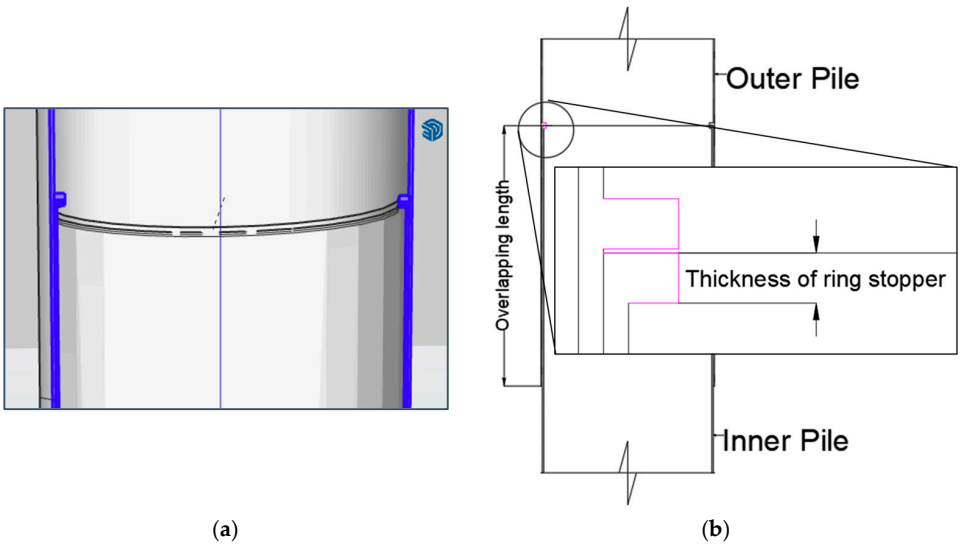

Figure 2. (**a**) Typical PIP slip joint arrangement, (**b**) 2D schematic detail of ring stopper.

2. Methodology

The method is based on the previously studied and verified model while analyzing the PIP slip joint for pure bending [11]. A finite element model was first prepared based on the previously verified modeling technique. The load is then applied to the prescribed boundary condition. For loading, the IEC-61400-3-1 has followed [13]. In order to carry out this simulation analysis, in this study ANSYS Mechanical 2023, R2 was used. Here, four different models were developed, three with different overlapping lengths and another one for only pile without any joints. The result can then be interpreted to create a desirable relationship.

2.1. Material Properties and Geometry

In this study, the CHS structure was modeled by using S-355 (equivalent to EN 10025-2) steel, as it is frequently used in structural applications nowadays. Nonlinear material properties were utilized to represent the real scenario in local buckling. The bi-linear hardening model was employed to replicate the nonlinear buckling.

The material properties are presented in the following Table 1.

Table 1. Material properties.

f_y (MPa)	E_t (MPa)	E (MPa)	υ	ρ (kN/m^3)
355	1450	210,000	0.3	76.98

Here, f_y is the yield stress, **E** is the modulus of elasticity, E_t is the tangent modulus, υ is the poisons ratio, and ρ is the density of the material.

When dealing with geometry, two different piles are considered to be overlapping with each other. If D represents the diameter of the inner pile, the overlapping lengths would be 1D, 2D, and 2.5D, respectively. In all three cases, the total length of the arrangement remains the same. A ring stopper is used in all three cases to provide stability against axial compression. The geometric properties are shown in Tables 2 and 3, which include the dimensions of the overlapping lengths of the ring stoppers. Based on a previous study by POSCO, it has been demonstrated that the strength of the material can remain consistent even with an increase in the steel section thickness of more than 16 mm [14]. The same principle has been applied to ensure uniform strength throughout the entire section in this study.

Table 2. Geometric properties.

Geometry	Value (mm)
Total length, L	50,000
Outer dia of inner pile, D_1	8000
Outer dia of outer pile, D_2	8160
Thickness of wall, t	80

Table 3. Summary of PIP arrangement.

ID	D (mm)		t (mm)		Thickness of Ring Stopper (mm)	Overlapping Length, L_o (mm)
	Outer Pipe	Inner Pipe	Outer Pipe	Inner Pipe		
1.5D	8160	8000	80	80	160	12,000
2D	8160	8000	80	80	160	16,000
2.5D	8160	8000	80	80	160	20,000

2.2. Boundary Conditions

In order to achieve the most accurate representation, the smaller diameter pipe was fixed at the bottom and the free end was positioned at the top of the larger diameter

pipe, as illustrated in Figure 3. The total length of the arrangement spans 50 m. The initial conceptual arrangement was made using the following considerations: 15 m was considered mud level, and another 20 m was considered water depth. The overlapping length (L_o) is placed exactly in the middle of the 50 m monopile structure. Initially, the fixed support condition was considered for the gradual development of the arrangement. In further studies, the complex support condition arising from soil-structure interaction can be used. A frictional contact was considered between larger and smaller diameter piles. Additionally, two-ring stoppers were used to resist axial compression, as shown in Figure 2.

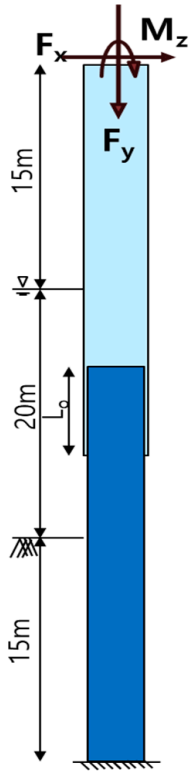

Figure 3. Idealized representation of the total arrangement.

The loading was carefully determined following the IEC-61400-3-1 [13]. After analyzing the various loading conditions for fixed onshore wind turbines, the idealized simplified loading was identified and applied to the arrangement, as depicted in Figure 3. All loading configurations can be found in Table 4.

Table 4. Load configuration.

Axial Compression (N)	Lateral Load (N)	Moment (N.mm)
1.989×10^7	5.392×10^6	5.2489×10^{11}

To impose remote forces, rigid "multi-point constraints" (MPCs) have been utilized, as depicted in Figure 4. The friction of the contact surface is a crucial factor when two piles overlap. The area where the piles come into contact is termed as a face-to-face frictional contact surface, as depicted in Figure 5. In this research, a frictional coefficient of 0.4 was used, following R.J.M. Pijpers et al. [15].

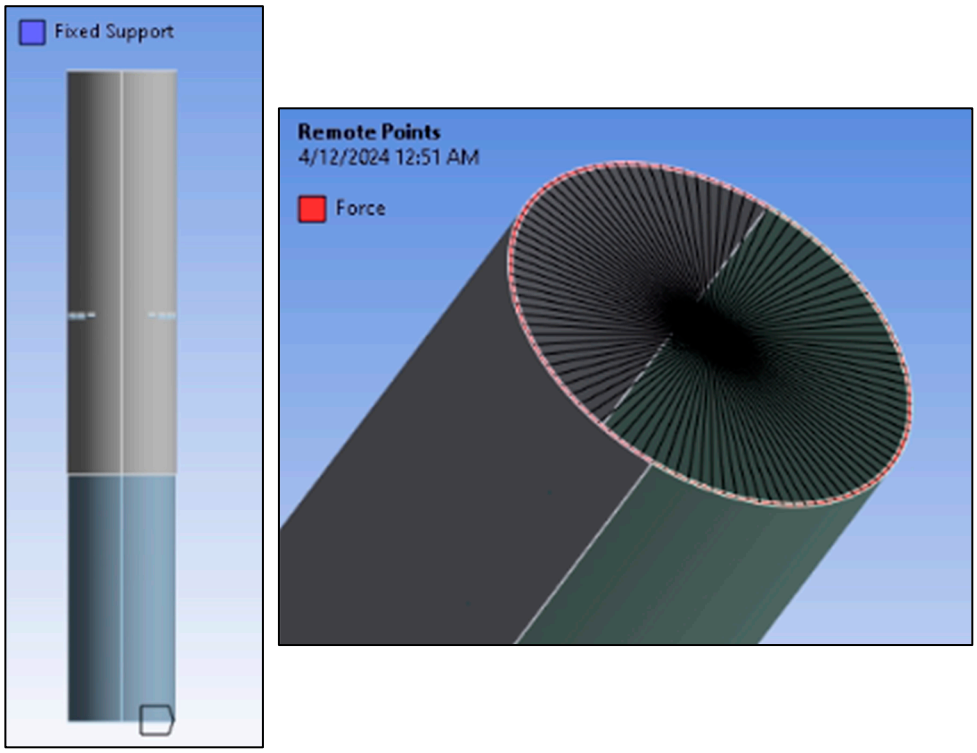

(**a**) (**b**)

Figure 4. (**a**) Fixed support at the bottom of the arrangement, (**b**) MPC restraints.

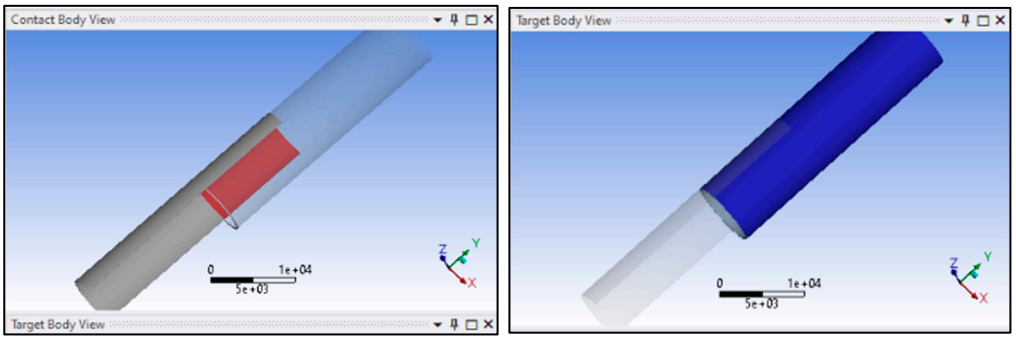

(**a**) (**b**)

Figure 5. (**a**) Contact surface and, (**b**) target surface for frictional contact.

2.3. Buckling Theories and Equations

The behavior of cylindrical shells under increasing local compression is crucial to understand and control. Differentiation between bifurcation and the limit buckling point is critical in this regard. Recent research in buckling theories has mainly focused on narrowing the gaps for engineering applications [16,17], with notable works by Koiter [18] and Donnell [19]. They addressed classical buckling analysis, introduced eigenvalue calculations for the "two-surface" model, and highlighted instability problems linked to geometrical imperfections. The imperfection amplitude is also calculated by paragraph 8.7 of Eurocode EN 1993-1-6 [20].

In Figure 6, a qualitative representation of the real behavior of an ideal section and a shell with imperfection is explained by showing the bifurcation points [21,22]. Moreover, the secondary bifurcation buckling paths, are shown as 2i, 2ii, 2iii, 3i, and 3ii to explain the idealized critical load factor of the structure, λ_{cr}. These values can be found through eigenvalue buckling analysis.

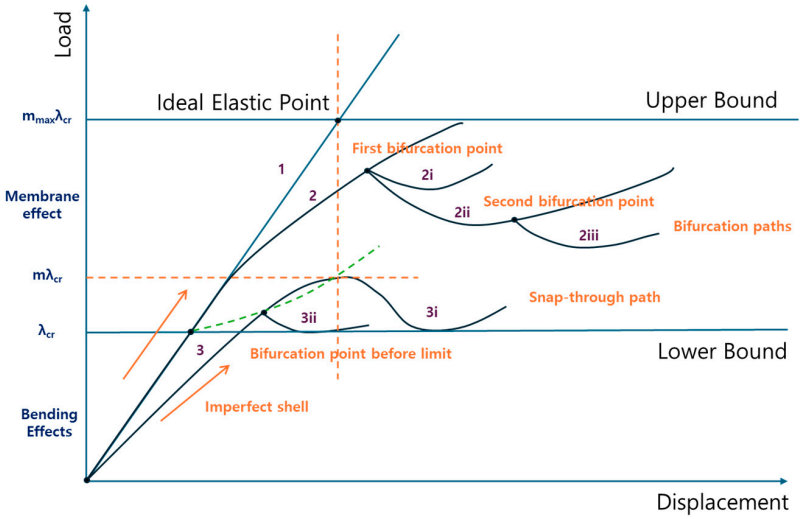

Figure 6. Types of buckling behavior.

When critical buckling happens, the load-displacement equilibrium path descends dramatically to a certain distance below the critical buckling load. Considering the above observations, multiple equilibrium paths are derived. In classical approaches, initial imperfections are factored into these equations, which can be resolved with existing algorithms to provide a single equilibrium path. The present investigation follows approximation to obtain the minimum point along the equilibrium path, aiming to identify the most realistic critical buckling load.

Through the analysis of different energy pathways and the use of the state of neutral equilibrium, this principle can be extended to the eigenvalue problem. This encompasses stiffness, geometries, and displacement matrices, including their linear and nonlinear components. Consequently, a simplified quadratic eigenvalue problem in the form [23,24] is revealed.

$$K_T V = K_e + \lambda^* \left(K_{gl} + K_{vl}\right) + \lambda^{*2}\left(K_{gn} + K_{vn}\right) V = 0 \quad (1)$$

$$\left(K_e + \lambda^* K_{gl}\right) V = 0 \quad (2)$$

Here,

K_e = initial elastic stiffness matrix,
K_{gl} = initial linear geometries matrix,
K_{vl} = respective matrix of linear displacements,
K_{gn} = initial geometrical stiffness matrix (quadratic form),
K_{vn} = initial displacement matrix (quadratic form), and
V = Nodal displacement vector.

Equations (1) and (2) approximate the classical eigenvalue problem by ignoring the shells' initial displacement. Incremental methods could solve the numerical problem through incremental load steps, whose equilibrium is checked iteratively. The solution of Equation (2) also relates to the critical load factor λ_{cr} depicted in Figure 6; λ^* is the eigenvalue solution of Equations (2) and (3), and is equal to λ_{cr} when it reaches its minimum value; this factor could, in turn, establish a relationship with a membrane and bending components (λ_m and λ_b, respectively), as follows:

$$\lambda_{ct} = \lambda_b + m \times \lambda_m \quad (3)$$

The membrane part λ_m is strongly linked to the total shell load-bearing capacity. It is worth highlighting that, in Figure 6, the upper and lower load bounds delimit realistic buckling performances as an extension of linear-elastic bending strength and as part of membrane effects developed by cylindrical shells [25].

2.4. Mesh Properties

In this study, a secondary mesh element HEX20 [26] was employed to uncover the full understanding of the local and total buckling. The term "HEX20 element" refers to a 20-node hexahedral element that exhibits quadratic displacement behavior. These 20 nodes offer an advanced capability to accurately represent the geometry and approximate the displacement field within the component (Figure 7). This feature is precious in structural engineering applications with high-stress gradients, such as in the vicinity of stress concentrations which is suitable for current study. In Table 5 the mesh statistics are provided.

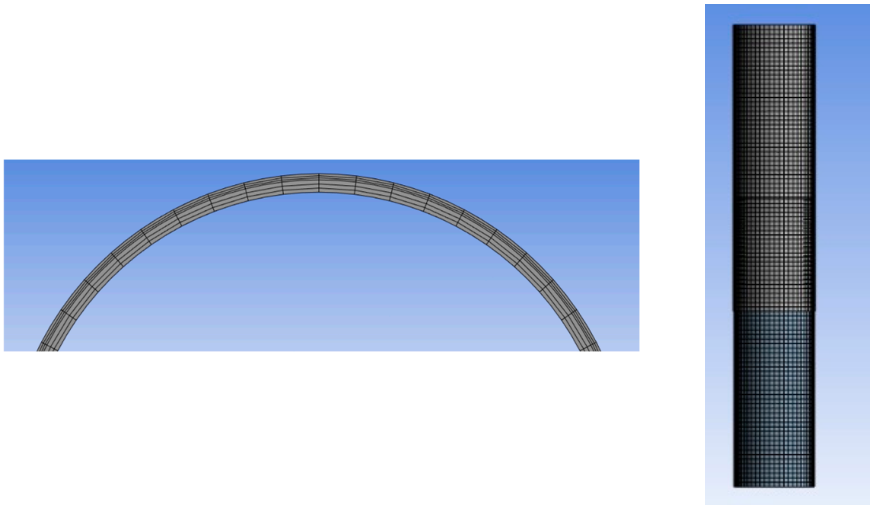

(**a**) (**b**)

Figure 7. (**a**) Meshing along the section of the pile, (**b**) total mesh arrangement along the longitudinal direction.

Table 5. Mesh statistics.

Total Element Nodes	101,661
Total Numbers of Elements	30,057
Mesh Metric	Jacobian Ratio (JR)
Avg. Value of JR	0.88765

2.5. Convergence

Globally, the assembly matrix is symmetric. Non-linear analysis default was used by Newton Raphson solution procedure (NROP). For rigid targeted surfaces, degrees of freedom on pilot nodes were selected. NROP was switched to an unsymmetrical solver (UNSYM) for frictional surfaces that encountered convergence difficulties [26]. The contact algorithm was chosen as the Augmented Lagrange method. Contact detection was performed at Gauss integration points. The contact stiffness factor was taken as 1. In analysis settings, sub-step controls were defined. The initial sub-step was set to 50. The minimum sub-step was also selected as 50, and the maximum sub-step was 1000. A total of 146 steps were used for convergence.

2.6. Verification

This study utilizes a validated model, previously published after peer review, to investigate the behavior of the PIP slip joint in pure bending. As the same boundary condition and overlapping length remain in this model, previous verification will also be reliable in this case. All the models without joint were developed using the same modelling techniques. In that study, the main focus was to replicate the force vs. displacement relationship

observed in another experimental analysis by Guo et al. [27] and the cantilever beam setup was validated. In the numerical analysis, displacement control loading was employed to ensure consistency with the experimental analysis. Table 6 provides the dimensions of the arrangement used for the validation. Figures 8 and 9 compare the experimental and validated numerical models. Figure 8 illustrates the ultimate deformed shapes from simulation models and compares them with those observed in experimental research. Based on the figure, it is apparent that the deformation shapes are identical. The difference between the FEA and experimental results for the cantilever beam was 17%, yet both exhibited almost identical trends. Several factors contributed to the discrepancy between the FEM analysis and experimental results. Firstly, the FEM model did not incorporate the influence of initial geometric imperfections, which can significantly impact structural behavior. Secondly, the material properties were simplified in the simulation by employing a bilinear hardening model, neglecting the complexities of real-world material response. Additionally, the boundary conditions implemented in the FEM analysis, utilizing rigid multi-point constraints to represent the stiffener plate, differed from the actual physical constraints, leading to potential variations in structural response. While the present model captures the essential behavior of the beams, it is important to note that precise replication of deflection and local buckling characteristics was also achieved. Consequently, the observed discrepancies in the previous study are considered justifiable due to these model limitations. The current study's model was developed based on the insights gained from this validated model.

Table 6. Dimensions of the model for verification.

ID	D (mm)	t (mm)	L (mm)	Boundary Condition
DT 100-3	200	2.00	1500	Cantilever beam

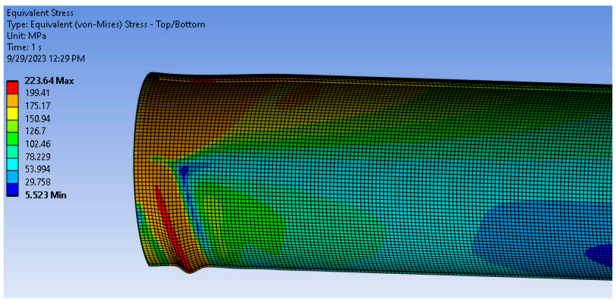

(**a**)

(**b**)

Figure 8. The deflection shape of a cantilever beam with a 100 D/t ratio. (**a**) Local buckling and rippling in the support area in the FEA model. (**b**) Similar local buckling in the experimental model for the cantilever beam. (Guo et al., 2013) [27].

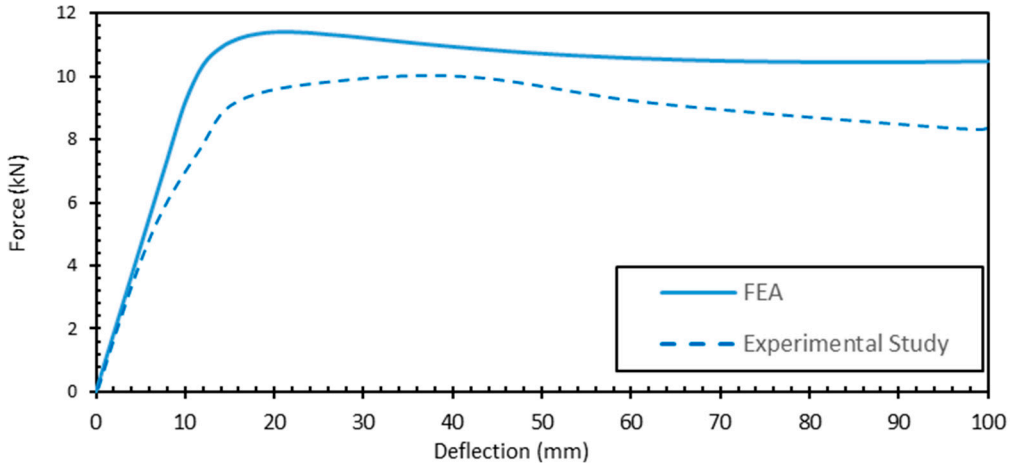

Figure 9. Force displacement relationship for the cantilever beam.

2.7. Limitations

Some limitations of the current study are detailed in this section. Nevertheless, it is important to note that these limitations do not diminish the validity of the study's results.

2.7.1. Initial Geometry

The initial geometric imperfections significantly impact the load-carrying capacity of models with different diameter-to-thickness (D/t) ratios. Moreover, there could also be a gap between the piles in practical scenarios. The current study did not consider any of the conditions.

2.7.2. Numerous Variables

Multiple variables, such as the length of the total pile arrangement, different material strengths, and D/t ratio, can affect the result of the current analysis. However, the current study only focuses on D/T ratios of 100 as it is a frequently used section, and the result is easily representable. However, this study will be carried out for different D/t ratios in the future.

2.7.3. Ovality Effect

The ovality of the PIP joint can significantly affect its performance, especially when subjected to bending loads.

2.7.4. Loading

This analysis does not consider any eccentric loading, which could introduce additional bending stresses along with axial stress. Furthermore, bi-axial bending and torsion were also not taken into account during analysis.

2.7.5. Frictional Coefficient

In this study, only one frictional coefficient was used [15]. The effect of different fictional coefficients was not considered.

Therefore, it is crucial to conduct additional research to understand better the behavior of the PIP slip joint under these diverse conditions.

3. Result and Discussion

After analysis, it has been determined that the overlapped area experiences significantly higher stress compared to other regions of the arrangement. Figure 10 illustrates the equivalent stress for the entire arrangement, revealing a consistent stress distribution. However, localized buckling is evident in the overlapped area, with the maximum deformation occurring at the free end of the arrangement. Notably, a visible gap between two

stoppers in the ring stopper area is causing a substantial concentration of stress in that specific area. Furthermore, the buckling effect has led to a noticeable change in the shape of the inner pile, as depicted in Figure 11b.

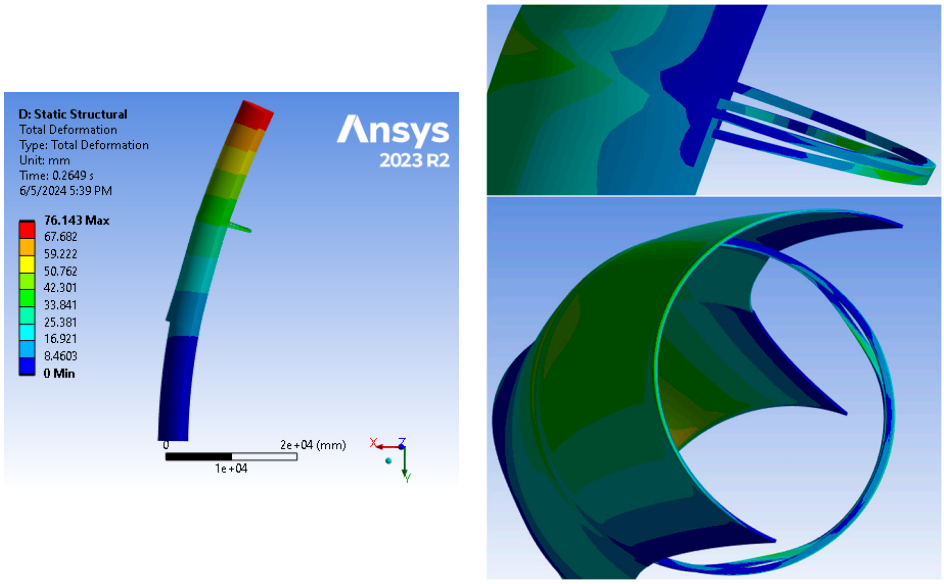

(**a**) (**b**)

Figure 10. (**a**) Deformation of the total configuration, (**b**) buckling and gap in the ring stopper.

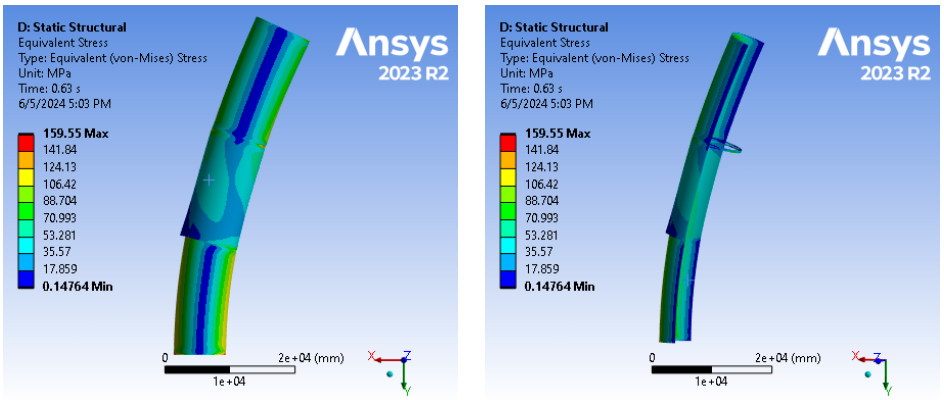

(**a**) (**b**)

Figure 11. (**a**) Equivalent von Mises stress, (**b**) sectional view of stress distribution in the arrangement.

The compression zone exhibited the highest stress, resulting in buckling in those regions. The maximum stress occurred at the interface of the inner and outer pile regions. When examining deformation, it was observed that the deflection was consistently varied from the support to the free end, as shown in Figure 11a. However, a notable change in deformation was observed after the overlapping area. Notably, a dent was also present in the ring stopper area, where it connects with the shell of the slip joint arrangement.

A more accurate condition assessment was obtained through meticulous analysis of the in the overlapped area, where stress concentration is known to occur. Additionally, contact pressure has also become a concern with the deformation in the ring stopper. However, introducing separate stiffeners can effectively mitigate these issues and make this topic a compelling one to address in the near future.

Valuable insights into pile-to-pile interaction were gained through a thorough examination of the frictional stress at the contact surface. These findings offer significant insights into the impact of frictional stress on load-bearing structures and suggest potential strate-

gies for optimizing the overall stability and load-bearing capacity of such arrangements [28]. Additionally, they serve as a crucial indicator of the load-transfer mechanism from the outer to inner piles. The potential to substantially enhance lateral resistance exists by strategically managing this frictional stress in the future. In Figure 12, the distribution of frictional stress is visually depicted, showing a higher concentration at the outer pile's edge (labeled as "zone B") where it intersects with the inner pile. A visible concentration of frictional stress at the edge of the inner pile, denoted as "zone A", was also observed. Notably, Figure 12b demonstrates a distinct behavior in the 2D overlapping length compared to the other two overlapping lengths in relation to frictional stress. The 2.5D and 1.5D overlapping lengths exhibit maximum frictional stress at 120 MPa and 116 MPa, respectively, while the 2D overlapping length peaks at 175 MPa. After a total displacement of 110 mm to 115 mm, a plateau in frictional stress was observed, followed by an increase up to 180 mm. This hike was caused by the very local deformation in the ring.

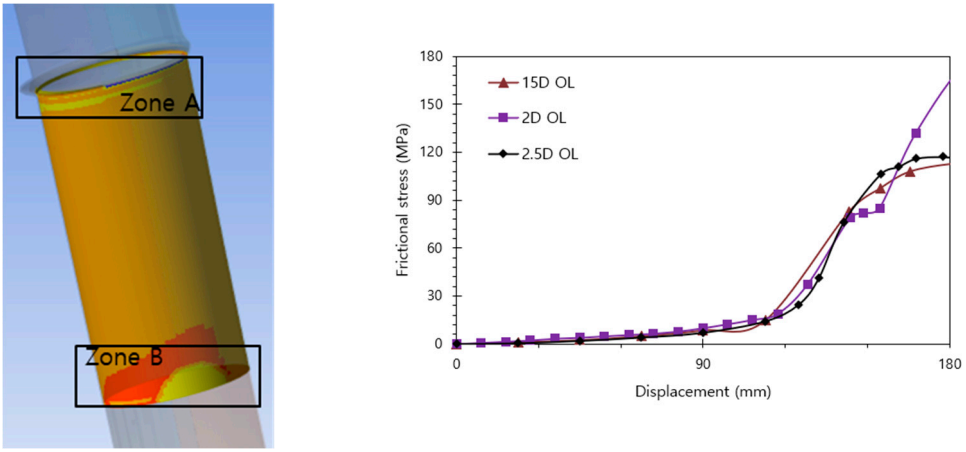

(**a**) (**b**)

Figure 12. (**a**) Frictional stress in the overlapped area, (**b**) comparison of frictional stress for different overlapping length.

While examining a sliding ring joint, the sliding distance study is obviously crucial. Longer sliding distances between surfaces lead to increased wear and material loss. The resulting sliding-induced fatigue cycles could significantly impact the components' lifespans in this slip joint configuration. This study plots the sliding distance between the ring stoppers of varying overlapping lengths against the total displacement. It is evident from Figure 13b that the sliding pattern is almost identical for 2D and 2.5D overlapping lengths, while the behavior is notably different for 1.5D overlapping lengths. The increase in sliding for 2D and 2.5D overlapping lengths compared to 1.5D overlapping lengths is 15% and 25%, respectively. This variance may be attributed to the rotation in the overlapped area, consequently causing lateral pressure on the ring and potential deformation.

Consequently, the distortion in the ring joint was also checked. The deformed ring stopper is shown in Figure 14a, and the pattern of deformation for different overlapping lengths is shown in Figure 14b. From the figures, it can be observed that although the 2.5D and 1.5D overlapping lengths have the same pattern for ring deformation, the maximum value of deformation is 59 mm and 48 mm, respectively. The 2D overlapping length, however, showcases interesting behavior. It peaked at 62 mm with a total deformation of 120 mm. Subsequently, it decreased with a negative slope until a total deformation of 150 mm. Beyond this point, it ascended to 180 mm of total arrangement, with the maximum deformation in the ring reaching 78 mm. The observation suggests that after 150 mm of total displacement, the ring experienced local buckling, resulting in a loss of integrity. Therefore, the need to investigate this local buckling further in future studies remains essential.

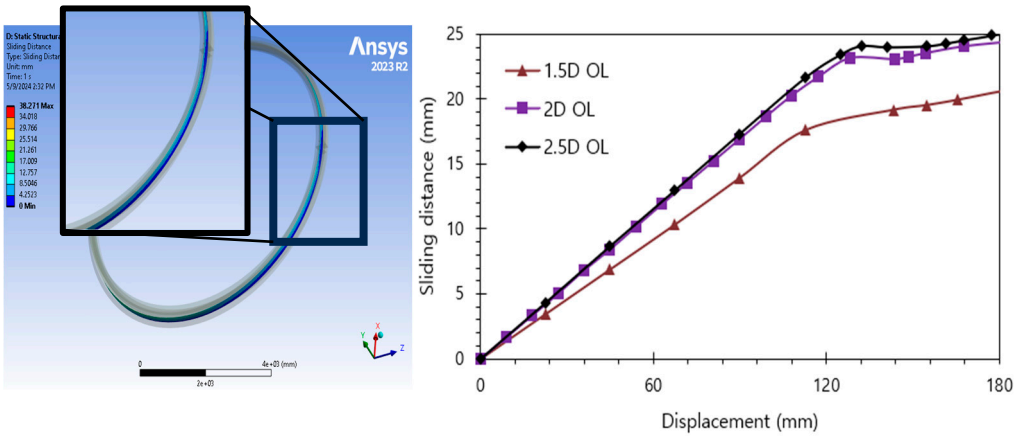

(**a**) (**b**)

Figure 13. (**a**) Sliding distance for two ring stoppers, (**b**) sliding distance vs. displacement for different overlapping lengths.

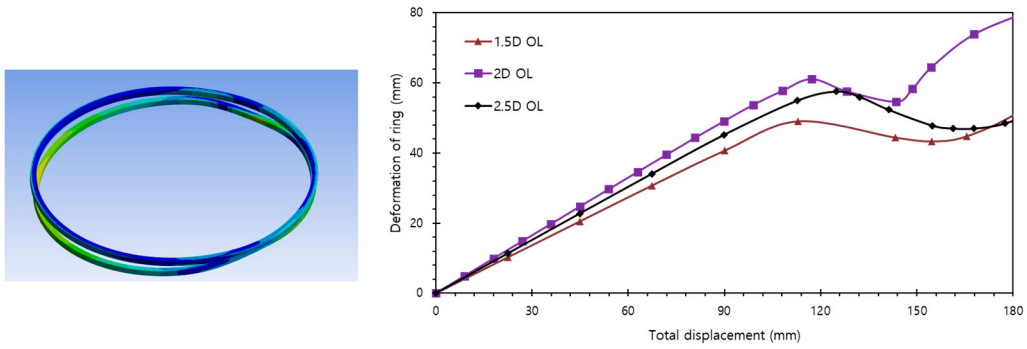

(**a**) (**b**)

Figure 14. (**a**) Deformation in the ring, (**b**) ring deformation vs. total displacement.

In order to evaluate the axial load and moment capacity in the ring stopper area, this study considered the area where both of these parameters are crucial. After analyzing, it was found that the area lies in the region with overlapping lengths. To improve the understanding of the scenario, a model of a pile without any joints was also analyzed and compared with the result of pile slip joint arrangements. Figure 15a,b present the axial load and moment capacity with respect to the normalized rotation. Figure 16 shows the location of moment and resisting axial load in the PIP slip joint arrangement. To understand the behavior of the PIP slip joint based on bending and compression, this location is optimum. The axial compression and moment capacities were plotted against the rotational ratio to normalize it with respect to a dimensionless parameter. Surprisingly, in terms of axial load-carrying capability, the single pile section exhibited better results than the PIP slip joint arrangements. Among the slip joint arrangements, the 2.5D configuration demonstrated the maximum axial load-carrying capacity, with the axial compression capacity for 2D and 1.5D being almost identical. The axial load carrying capacity of 2.5D is nearly 5% more than the other two configurations, while in the case of the only pile, it exhibited a 9% resistance against the axial load. This might be attributed to stress concentration in a smaller region of the ring stopper area.

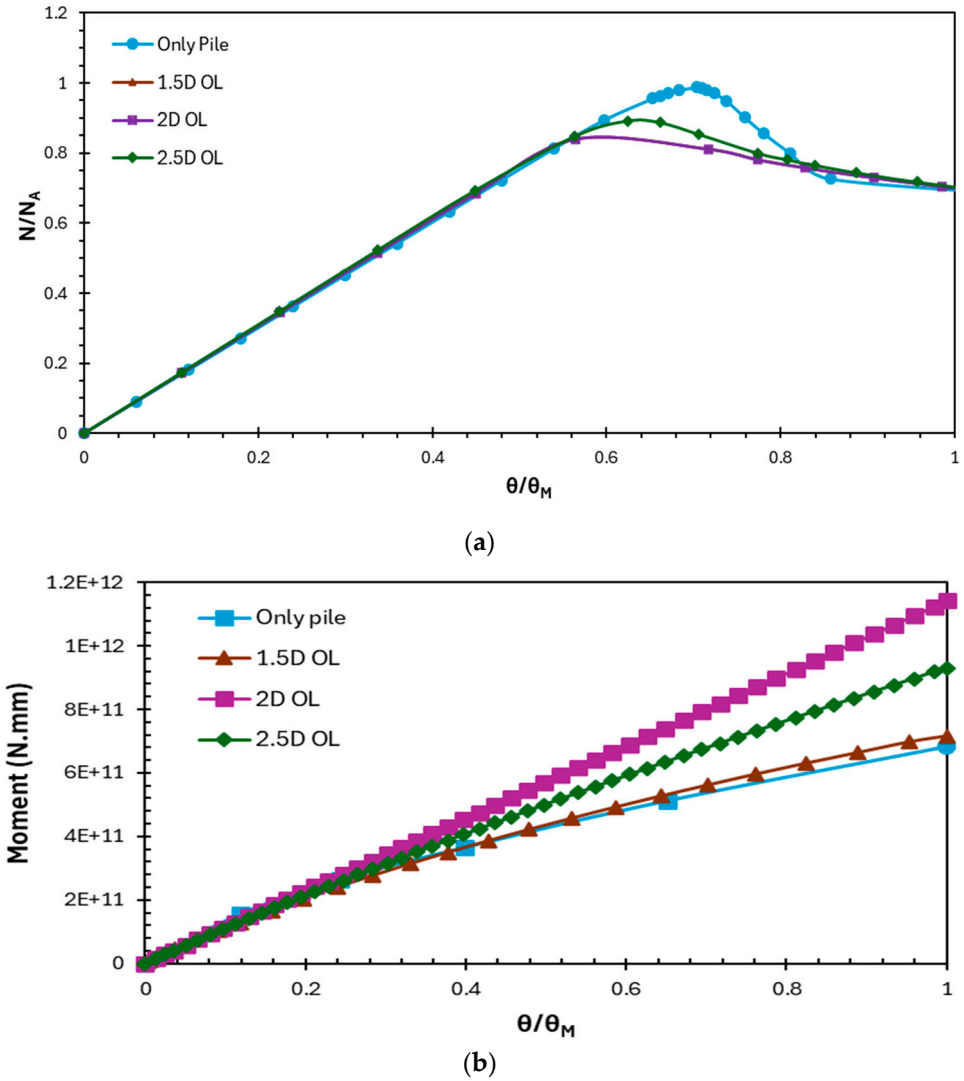

Figure 15. (**a**) Axial load vs. normalized rotation, (**b**) moment vs. normalized rotation.

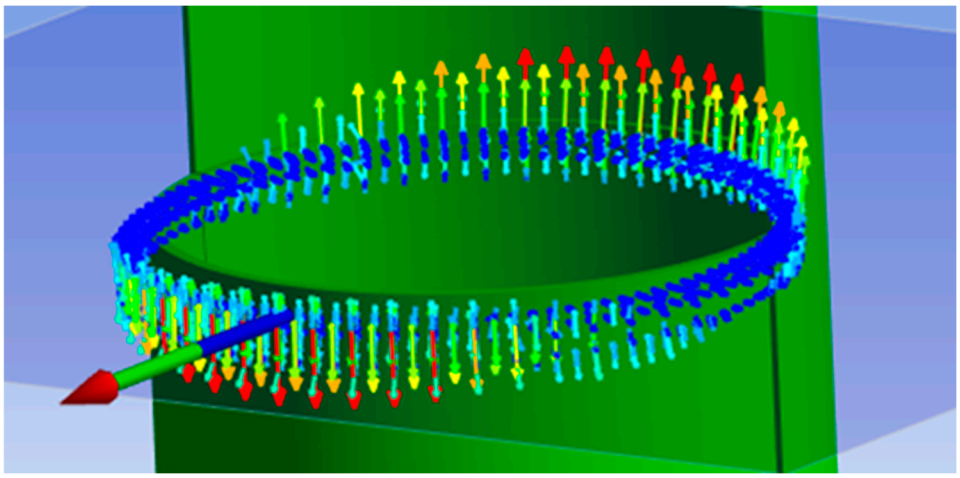

Figure 16. Axial load and moment in the ring stopper area.

On the other hand, for moment capacity, the PIP slip joint has better moment capacity than the single pile section. Among the three different overlapping lengths, the 2D overlapping length provides better rotational resistance than the other two configurations.

Following that, the 2.5D and 1.5D overlapping length arrangements have a greater capability of resisting rotation in chronological order. The rotational capacity for 1.5D, 2.5D, and 2D overlapping lengths is 4.77%, 36.02%, and 67.14% more than the single pipe case. The moment capacity increased significantly due to the change in stiffness around the overlapping area.

Based on this analysis the normalized compression-moment envelopes are presented in Figure 17. Here, N_y and M_y represent the maximum axial load and the yield moment of the section. All the curves for the slip joint arrangements are nearly straight lines. To compare with the NORSOK code, a shaded area is also marked in graph. Within that area every line satisfies the design criteria proposed by the code. In all the cases, the lines lie within that area.

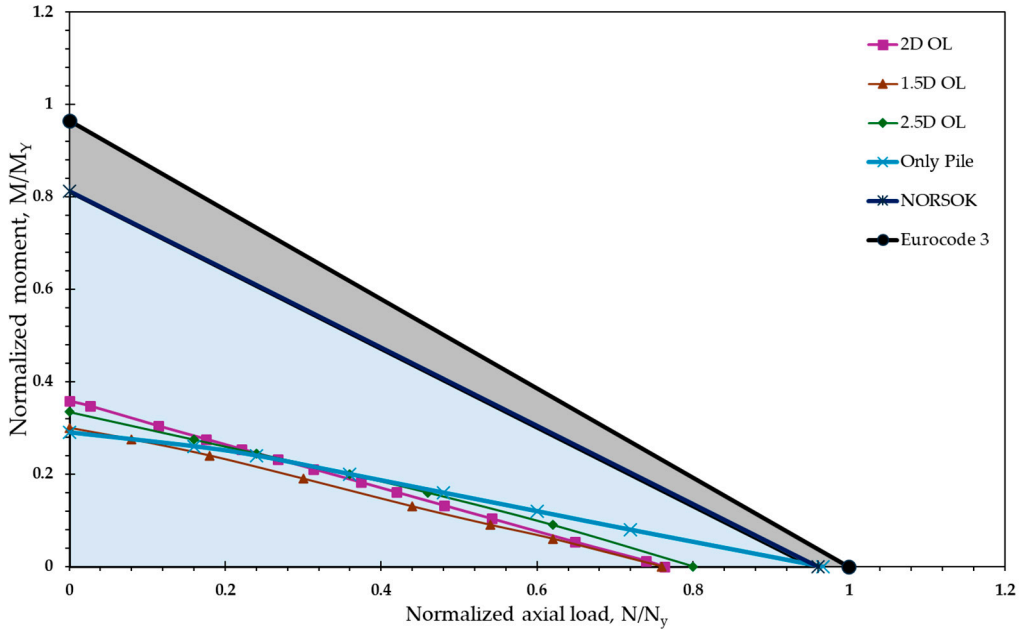

Figure 17. Moment compression envelops.

From the aforementioned analysis and discussion, it was found that the slip joint arrangement has to be designed to satisfy the following estimated equation.

$$\frac{N_{SD} * \gamma_D}{N_y * \left(A * f_y / f_{CLE}\right)} + \frac{M_{SD} * \gamma_D}{M_y * \left[B * \left(D * f_y\right) / \left(t * E\right)\right]} \leq 1 \quad (4)$$

In the "NORSOK N-004" code (Section 7.3) the equations are presented as follows [12]:

$$\frac{N_{SD} * \gamma_D}{N_y * \left(1.047 - 0.274 * f_y / f_{CLE}\right)} + \frac{M_{SD} * \gamma_D}{M_y * \left[0.94 - \left(0.76 * D * f_y\right) / \left(t * E\right)\right]} \leq 1 \quad (5)$$

Here,

- N_{SD} and M_{SD} are the design axial compression and design bending moment.
- N_y and M_y are the axial load capacity and yield moment, respectively.
- A and B are two dimensionless constants.
- D and t are the diameter and the thickness of the section.
- f_y and E are the yield strength and the Young's modulus.
- C_e and γ_D are the elastic buckling coefficient (0.3) and material factor, respectively.
- f_{CLE} is the characteristic elastic local buckling.

Both equations are applicable for the following conditions:

$$0.1034 < {}^{D*f_y}/_{E*t} < 120 f_y/E$$
$$0.170 < f_y/f_{CLE} < 1.911$$
$$f_{CLE} = 2 * C_e.E * {}^{t}/_{D}$$

In Equation (4) for different values of A and B the general design equation can be found for three different overlapping lengths. For different D/t ratios, these values will be different, and the P-M curves will be shifted parallel to the top and bottom of the current curves. In Table 7 the values of these constants have been given for different overlapping lengths.

Table 7. Values of A and B for different overlapping lengths.

Overlapping Length (OL)	A	B
1.5D	2.48	1.775
2D	2.698	2.117
2.5D	2.8399	1.99

The members that are subjected to combined bending and axial compression need to satisfy the following condition as per Eurocode 3 (Section 6.3, Part 1-1) for a class-4 section [20]:

$$\frac{N_{ED}}{\chi_y.N_{Rk}/\gamma_{MI}} + k_{yy}\frac{M_{y.ED}}{\chi_y.M_{y.Rk}/\gamma_{MI}} \leq 1 \quad (6)$$

Here,

- N_{ED} and $M_{y\cdot ED}$ are the design axial compression and design bending moment.
- N_{Rk} and $M_{y\cdot Rk}$ are the design value of the resistance depending upon the section.
- χ_y is reduction factor due to flexural buckling.
- k_{yy} is the interaction factor.

Based on the findings, it is evident that PIP slip joints outperform tubular sections without a joint in flexure. However, it is possible to develop the PIP slip joint using alternative methods for axial compression. Previous research has shown that in the case of pure bending, the 2D overlapping length outperforms the other two slip joint arrangements. This finding remains consistent when considering combined loading.

4. Conclusions

The current study explores structural analysis of the PIP slip joints, particularly focusing on stress distribution, deformation, and load-bearing capacities under axial compression and bending moments. The study observes that the overlapped area of the joint arrangement is prone to higher stress levels, leading to localized buckling and deformation.

Frictional stress at the contact surface is also being studied to understand how it affects the structural behavior and load-transfer mechanism. The distribution of frictional stress indicates higher concentrations at specific zones where the outer and inner piles intersect. The 2D overlapping length stands out for reaching a peak frictional stress of 175 MPa, and a plateau is followed by an increase in stress after certain displacement thresholds.

The study also analyzed the sliding distance between ring stoppers and found that longer overlapping is associated with higher wear and potential deformation. The sliding patterns of 2D and 2.5D overlapping lengths are similar, while the 1.5D length behaves differently. This difference is due to rotation in the overlapped area, which applies lateral pressure on the ring.

The deformation of the ring joint was also investigated and found that the 2D overlapping length exhibited a distinct pattern of deformation, reaching a peak of 62 mm then decreasing before rising again. This indicates the occurrence of local buckling and gap

formation after a specific displacement point, resulting in a loss of structural integrity. Additionally, a general design equation has been estimated and compared with NORSOK and Eurocode for the same condition. The findings are significant for designing and analyzing PIP slip joints, offering a comprehensive understanding of their structural behavior under various loading conditions.

For further expansion of the current study, it is deemed to have an experimental analysis for validating the current study of PIP slip joint designs. Moreover, varying D/t ratios, load distances, and eccentricities are other focal points to be developed.

Author Contributions: Conceptualization, M.A.I. and D.L.; methodology, M.A.I. and D.L.; soft-ware, M.A.I. validation, M.A.I., and D.L.; investigation, M.A.I. and D.L.; data curation, M.A.I., S.A. and H.P.; writing—original draft preparation, M.A.I.; writing—review and editing, M.A.I., S.A., H.P. and D.L. visualization, M.A.I. and S.A.; supervision, D.L. All authors have read and agreed to the published version of the manuscript.

Funding: This work was supported by the Human Resources Development of the Korea Institute of Energy Technology Evaluation and Planning (KETEP) grant funded by the Korean government (Ministry of Trade, Industry and Energy) (No. 20214000000180), and the Korea Institute of Energy Technology Evaluation and Planning (KETEP) grant funded by the Korea government (MOTIE) (20224000000220, Jeonbuk Regional Energy Cluster Training of human resources).

Institutional Review Board Statement: Not applicable.

Informed Consent Statement: Not applicable.

Data Availability Statement: The data presented in this study are available on request from the corresponding author.

Conflicts of Interest: The authors declare no conflict of interest.

References

1. Nasab, N.M.; Kilby, J.; Bakhtiaryfard, L. Analysis and Design of Monopile Foundations for Offshore Wind and Tidal Turbine Structures. *Water* **2022**, *14*, 3555. [CrossRef]
2. Ali, S.; Lee, S.-M.; Jang, C.-M. Techno-Economic Assessment of Wind Energy Potential at Three Locations in South Korea Using Long-Term Measured Wind Data. *Energies* **2017**, *10*, 1442. [CrossRef]
3. Schaumann, P.; Böhm, M.; Schürmann, K. Improvements in the fatigue design of support structures for offshore wind turbines. *Steel Constr.* **2021**, *14*, 74–82. [CrossRef]
4. *DNV-ST-0126*; Support Structures for Wind Turbines. DNV GL AS.: Bærum, Norway, 2021. Available online: https://www.dnv.com/energy/standards-guidelines/dnv-st-0126-support-structures-for-wind-turbines/ (accessed on 16 November 2022).
5. Varun Bhat, I.K.; Prakash, R. LCA of renewable energy for electricity generation systems—A review. *Renew. Sustain. Energ. Rev.* **2009**, *13*, 1067–1073. [CrossRef]
6. Blanco, M.I. The economics of wind energy. *Renew. Sustain. Energ. Rev.* **2009**, *13*, 1372–1382. [CrossRef]
7. Ummenhofer, T.; Boretzki, J.; Albiez, M. Hybrid connection technologies for hollow sections in steel construction. *Steel Constr.* **2022**, *15*, 37–50. [CrossRef]
8. *ASME B16.5-2020*; Pipe Flanges and Flanged Fittings: NPS 1/2 through NPS 24 Metric/Inch Standard. American Society of Mechanical Engineers (ASME): New York, NY, USA, 2020.
9. Tran, T.-T.; Park, H.; Lee, D. Structural Behavior of L-Type Flange Joint with Various Flange Flatness Conditions. *Energies* **2023**, *16*, 5703. [CrossRef]
10. Ahmadi, H.; Mayeli, V. Probabilistic analysis of the local joint flexibility in two-planar tubular DK joints of offshore jacket structures under in-plane bending loads. *Appl. Ocean Res.* **2018**, *81*, 126–140. [CrossRef]
11. Islam, M.A.; Park, H.; Lee, D. Structural Behavior of a PIP Slip Joint under Pure Bending Considering Nonlinear Buckling. *Energies* **2024**, *17*, 35. [CrossRef]
12. *NORSOK N-004:2022*; Design of Offshore Structures. Norwegian Oil and Gas Association: Harstad, Norway, 2022.
13. *IEC 61400-3-1:2019*; Wind Energy Generation Systems—Part 3-1: Design Requirements for Fixed Offshore Wind Turbines. IEC: Geneva, Switzerland, 2019.
14. POSCO Research Team. High-Performance, Low-Cost POSCO GigaSteel Welding Technology Research Paper Published in Nature Communications. *POSCO Newsroom*, 20 February 2024.
15. Pijpers, R.J.M.; Slot, H.M. Friction coefficients for steel-to-steel contact surfaces in air and seawater. *J. Phys. Conf. Ser.* **2020**, *1669*, 012002. [CrossRef]

16. Teng, J.G.; Rotter, J.M. Cylindrical shells under axial compression. In *Buckling of Thin Metal Shells*; CRC Press: Boca Raton, FL, USA, 2006; pp. 42–87.
17. Hu, N.; Burgueño, R. Buckling-induced smart applications: Recent advances and trends. *Smart Mater. Struct.* **2015**, *24*, 063001. [CrossRef]
18. Koiter, W. The Stability of Elastic Equilibrium. Ph.D. Thesis, University of Delft, Delft, The Netherlands, 1970.
19. Donnell, L.H.; Wan, C.C. Effects of Imperfection on Buckling of Thin Cylinders and Columns under Axial Compression. *J. Appl. Mech.* **1950**, *17*, 73–83. [CrossRef]
20. *EN 1993-1-6*; Eurocode 3: Design of Steel Structures. Part 1-6: Strength and Stability of Shell Structures. European Commission: Brussels, Belgium, 2007.
21. Yuan, L.; Zhou, J.; Yu, Z.; Xu, W. Numerical investigation of buckling behavior of dented lined pipe under bending. *Int. J. Press. Vessel. Pip.* **2023**, *205*, 104997. [CrossRef]
22. Langhaar, H.L. Theory of Buckling. In *Energy Methods in Applied Mechanics*; Dover Publications: New York, NY, USA, 2016; pp. 201–232.
23. Eslami, M.R. *Buckling and Post buckling of Beams, Plates, and Shells*; Springer Science and Business Media LLC: Berlin/Heidelberg, Germany, 2018; pp. 381–464.
24. Aliabadi, M.H.; Falzon, B.G.; Scientific, W. The Development of Shell Buckling Design Criteria Based on Initial Imperfection Signatures. In *Buckling and Post Buckling Structures: Experimental, Analytical and Numerical Studies*; Imperial College Press: London, UK, 2008; pp. 99–140.
25. Calladine, C.; Sanders, J. Buckling of shells: Classical analysis. In *Theory of Shell Structures*; Cambridge University Press: Cambridge, UK, 1984; pp. 473–542.
26. *ANSYS Mechanical*, version 2023R2; ANSYS Mechanical Guideline; ANSYS, Inc.: Canonsburg, PA, USA, 2023.
27. Guo, L.; Yang, S.; Jiao, H. Behavior of thin-walled circular hollow section tubes subjected to bending. *Thin-Walled Struct.* **2013**, *73*, 281–289. [CrossRef]
28. Wu, Y.; Ren, Y.; Liu, J.; Ma, L. Analysis of Negative Skin Friction on a Single Pile Based on the Effective Stress Method and the Finite Element Method. *Appl. Sci.* **2022**, *12*, 4125. [CrossRef]